

MATERIALS SCIENCE

How heteroepitaxy occurs on strontium titanate

Seyoung Cook^{1,2}, Kendra Letchworth-Weaver^{3*}, I-Cheng Tung⁴, Tassie K. Andersen^{1,2}, Hawoong Hong⁴, Laurence D. Marks², Dillon D. Fong^{1†}

In traditional models of heteroepitaxy, the substrate serves mainly as a crystalline template for the thin-film lattice, dictating the initial roughness of the film and the degree of coherent strain. Here, performing in situ surface x-ray diffraction during the heteroepitaxial growth of LaTiO₃ on SrTiO₃ (001), we find that a TiO₂ adlayer composed of the $(\sqrt{13} \times \sqrt{13})R33.7^\circ$ and $(\sqrt{2} \times \sqrt{2})R45.0^\circ$ reconstructions is a highly active participant in the growth process, continually diffusing to the surface throughout deposition. The effects of the TiO₂ adlayer on layer-by-layer growth are investigated using different deposition sequences and anomalous x-ray scattering, both of which permit detailed insight into the dynamic layer rearrangements that take place. Our work challenges commonly held assumptions regarding growth on TiO₂-terminated SrTiO₃ (001) and demonstrates the critical role of excess TiO₂ surface stoichiometry on the initial stages of heteroepitaxial growth on this important perovskite oxide substrate material.

INTRODUCTION

The development of a preparation method to consistently produce an atomically flat SrTiO₃ (STO) (001) surface (1) was a major milestone in enabling the growth of perovskite epitaxial thin films. This method, and modified versions of this method (2–5), involves the removal of SrO at the surface by a chemical means, ensuring an atomically smooth, TiO₂-terminated surface by annealing in an oxidizing environment. The resulting surface exhibits a step-and-terrace morphology with step heights equivalent to one STO unit cell (~0.4 nm) (Fig. 1A). It is typically assumed that the prepared STO substrate is terminated by a single TiO₂ plane on the basis of the surface morphology and the 1 × 1 diffraction pattern obtained by in situ reflection high-energy electron diffraction in the growth chamber.

TiO₂-terminated STO is ideal for the epitaxial growth of ABO₃ perovskite materials, as it allows continuation of the AO-BO₂ stacking sequence along [001], provided that one uses a digital synthesis technique such as oxide molecular beam epitaxy (MBE) (Fig. 1B) (6–8). The importance of being able to precisely control layering on the atomic level cannot be overstated, as it has been key to the discovery of quantum phases and a variety of emergent phenomena at the interface between STO and other complex oxides (9–17). For instance, a number of research groups have discovered two-dimensional electron gas (2DEG) formation and even superconductivity (18) at the TiO₂-terminated interface between LaAlO₃ and STO but not at the SrO-terminated one (19). The behavior is strongly thickness dependent, with the 2DEG arising only for LaAlO₃ films that are four unit cells or thicker; heterostructures with a thickness of three unit cells remain insulating (20, 21). Using digital pulsed laser deposition (PLD), Jang *et al.* (22) found that inserting a single layer of RO (where R is a rare-earth element) between the TiO₂ layers of STO also led to 2DEG formation and local electron correlations. In more recent years, high-temperature superconductivity has also been discovered in single-layer FeSe films grown specifically on the TiO₂-terminated STO (001) surface (23, 24).

¹Materials Science Division, Argonne National Laboratory, Argonne, IL 60439, USA.

²Department of Materials Science and Engineering, Northwestern University, Evanston, IL 60202, USA. ³Center for Nanoscale Materials, Argonne National Laboratory, Argonne, IL 60439, USA. ⁴X-ray Science Division, Argonne National Laboratory, Argonne, IL 60439, USA.

*Present address: Department of Physics and Astronomy, James Madison University, Harrisonburg, VA 22807, USA.

†Corresponding author. Email: fong@anl.gov

However, this surface can be structurally complex, given the multitude of surface reconstructions that have been discovered [reviewed in (25) and references therein]. The atomic structures of many of these reconstructions have been solved (26–30), and these surfaces are known to be Ti rich (31). That is, most of these surfaces are terminated by a TiO₂ double layer (DL), consisting of a TiO₂ adlayer formed by corner- and edge-sharing TiO₅□ octahedral units (where □ is a vacant site) residing atop a bulk-like TiO₂ plane (29). Furthermore, given the local network structure of the (001) reconstructions featuring recurrent structural motifs and their similar surface energies (29, 30, 32), it is likely that this surface is a 2D glass composed of several different TiO₂ DL reconstructions.

In this work, we use oxide MBE with in situ surface x-ray diffraction (SXRD) to investigate the surface of (001)-oriented STO and study the effects of the surface structure on the initial stages of LaTiO₃ heteroepitaxial growth. Although LaTiO₃ is a Mott-Hubbard insulator and STO is a band insulator (33), the LaTiO₃/STO system exhibits metallic conductivity (9) and is a well-known system for probing charge modulation at the atomic scale (34). We find the presence of a TiO₂ DL and observe that the atomic planes continuously rearrange during LaTiO₃ deposition, challenging commonly held assumptions regarding layer-by-layer growth on STO (001) and providing a new model for engineering interfacial phenomena in the complex oxides.

RESULTS AND DISCUSSION

The STO substrates were prepared by the standard etch-and-anneal method as described in (2) (see Methods). This procedure yields the atomically smooth, step-and-terrace surfaces shown in Fig. 1A and fig. S1. We determined the out-of-plane structure of the (001) substrate immediately before heteroepitaxial growth by measuring the specular rod under both nonresonant (NR) (15.0 keV) and resonant (R) conditions (16.1 keV, near the Sr K-edge) (35). The structure was determined by simultaneous fitting of the NR and R specular rods using a density functional theory (DFT)-constrained procedure (36), as described in section S2.

The results for two different substrates are presented in Fig. 2 (A and B), where the momentum transfer q is expressed in terms of reciprocal lattice units (r.l.u.) referenced to the STO room temperature lattice parameter. As observed, there are substantial differences between the

Copyright © 2019
The Authors, some
rights reserved;
exclusive licensee
American Association
for the Advancement
of Science. No claim to
original U.S. Government
Works. Distributed
under a Creative
Commons Attribution
NonCommercial
License 4.0 (CC BY-NC).

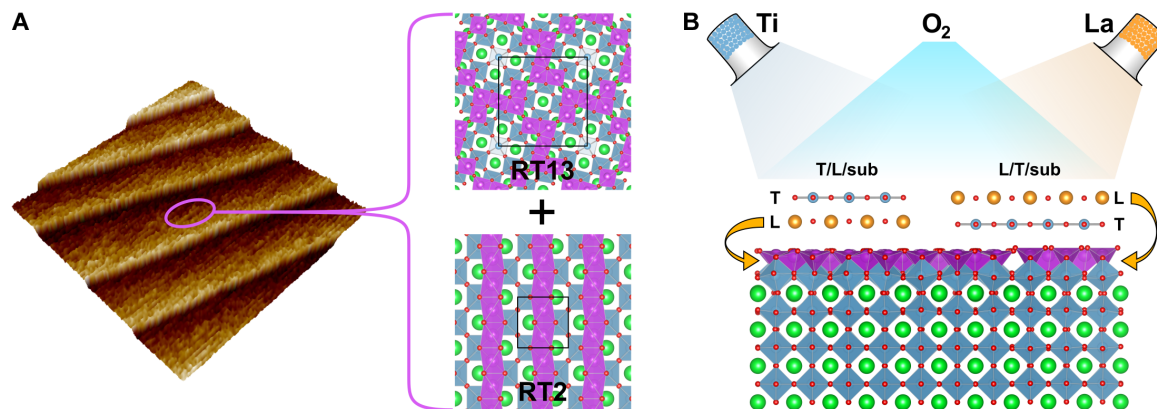


Fig. 1. Depiction of the STO surface and its behavior during epitaxial growth. (A) Bare STO (001) surface after following the standard etch-and-anneal procedure, exhibiting ~ 0.4 -nm-high steps with both $(\sqrt{13} \times \sqrt{13})R33.7^\circ$ (RT13) and $(\sqrt{2} \times \sqrt{2})R45.0^\circ$ (RT2) surface reconstructions. (B) Schematic of LaTiO_3 growth by oxide MBE following either the TiO_2/LaO (T/L) or LaO/TiO_2 (L/T) growth sequence at 700°C in a background of 1×10^{-7} torr O_2 .

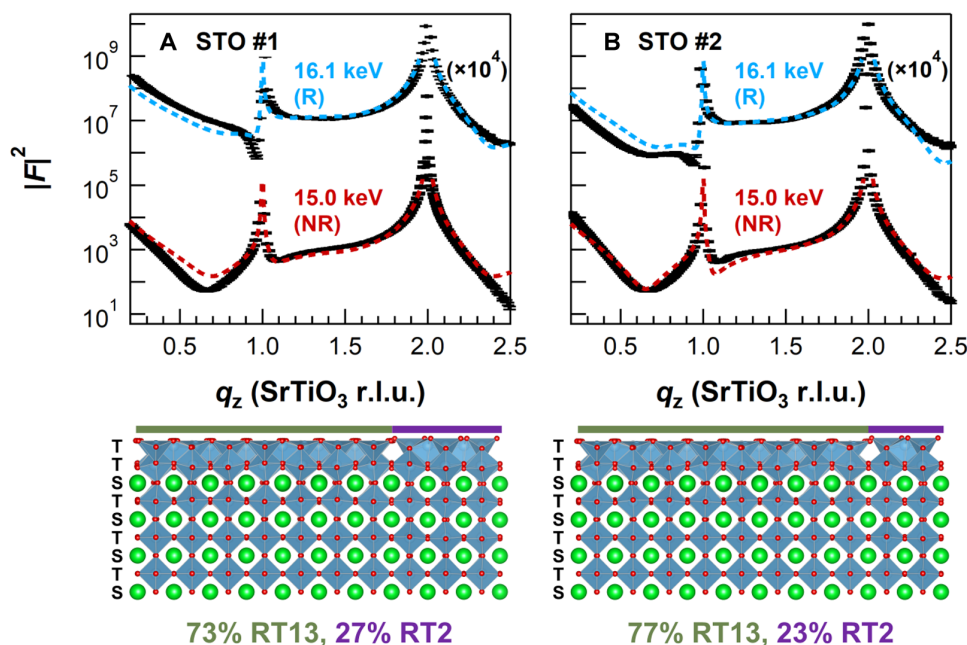


Fig. 2. The atomic structures of STO surfaces. Fitted specular reflectivity curves (top) for the bare (001) STO substrates modeled using mixtures of the $(\sqrt{13} \times \sqrt{13})R33.7^\circ$ (RT13) (29) and $(\sqrt{2} \times \sqrt{2})R45.0^\circ$ (RT2) (37) reconstructions (below). DFT-constrained fit results (dashed lines) for the bare STO #1 (A) and STO #2 (B) substrates. The intensity is given by the square of absolute x-ray structure factor ($|F|^2$). Points near the Bragg peaks were excluded from the fits.

NR and R spectra, particularly near the 001 reflection: The R spectrum exhibits a local minimum below the 001 reflection, while the NR spectrum exhibits a local minimum above the 001 reflection. This difference originates from the TiO_2 DL, and fitting permits a quantitative measure of its coverage. The fits indicate that the TiO_2 adlayer has a coverage of $\sim 80\%$, as modeled by a 3:1 mixture of two different (local) reconstructions: $(\sqrt{13} \times \sqrt{13})R33.7^\circ$ (RT13) (29) and $(\sqrt{2} \times \sqrt{2})R45.0^\circ$ (RT2) (37). We note here that RT13 and RT2 represent the lowest-energy surface structures in terms of a convex hull construction for STO (001) (29). They are composed of different recurrent structural motifs found in other TiO_2 DL STO (001) reconstructions (32) and appropriately model the STO surface as a glass (section S2).

We subsequently deposited one unit cell of LaTiO_3 atop the TiO_2 DL STO by oxide MBE. As noted above, this is an oxide system that has

garnered considerable attention: Although both are insulators, the interface between them has demonstrated both metallic (9, 10) and superconducting (38, 39) behaviors, sparking widespread interest in understanding interfacial properties in the complex oxide community (19, 40–42). Individual monolayers (MLs) of LaO and TiO_2 were deposited on STO substrates via two distinct layer sequences. On substrate STO #1, 1 ML of TiO_2 was deposited atop 1 ML of LaO (T/L); on substrate STO #2, 1 ML of LaO was deposited atop 1 ML of TiO_2 (L/T). In Fig. 3 (A and B), we present the specular rods measured in situ at 700°C in 1×10^{-7} torr O_2 following the deposition of each ML under the T/L and L/T deposition sequences, respectively. As expected, the initial deposition of either LaO or TiO_2 on the TiO_2 DL STO (001) surfaces results in different specular reflectivity curves (lower NR and R curves in Fig. 3). The subsequent deposition of TiO_2 or LaO results in nearly

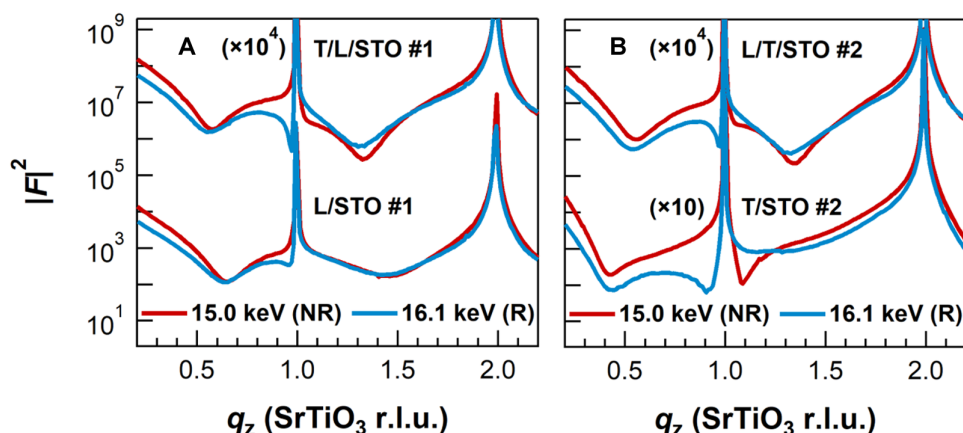


Fig. 3. Specular reflectivity curves after deposition of LaO and TiO₂ MLs for different deposition sequences. The results for T/L/STO #1 and L/T/STO #2 are shown in (A) and (B), respectively. Measurements were performed with x-ray energies of 15.0 keV (red) and 16.1 keV (blue) for scattering under NR and R conditions at the Sr K-edge, respectively. Note the nearly identical reflectivity curves following the two different deposition sequences, which indicate the rearrangement of atomic layers.

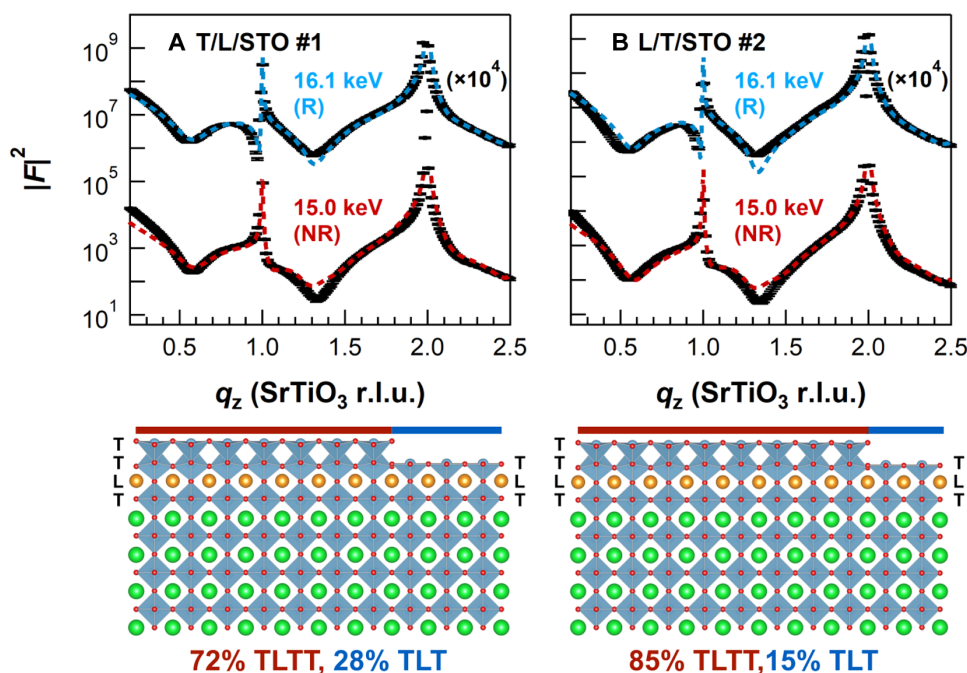


Fig. 4. Fitted specular reflectivity curves (top) for the final structures after the T/L/STO #1 and L/T/STO #2 depositions modeled as mixtures of the TLTT and TLT surface structures (bottom). Fit results are presented as dashed lines for the T/L/STO #1 (A) and L/T/STO #2 (B) final structures. Points near the Bragg peaks were excluded from the fits.

identical reflectivity curves, regardless of x-ray energy (upper NR and R curves in Fig. 3).

To determine the final structures after both LaO and TiO₂ deposition, we first calculated the specular reflectivity curves directly from DFT-determined surface structures. Using the nomenclature in which the layers progress from surface to bulk (SrO-terminated STO), these would be LaO/TiO₂/TiO₂/TiO₂/(SrO) or LTTT and, similarly, TLTT, TTLT, LTT, TLT, and TTL. These structures and the corresponding calculated specular reflectivity curves are presented in fig. S4.

We proceeded to fit the four upper curves in Fig. 3 (A and B) following the same DFT-constrained fitting procedure used for the bare STO (001) surfaces. A linear combination of the TLTT and TLT model

structures provides the best agreement with the specular reflectivity data, with the results shown in Fig. 4. Similar to the case of the bare substrate, the NR and R specular rods are highly distinctive and sensitive to the exact compositional arrangement at the surface owing to the high phase contrast between the different layers near an absorption edge. The final structures were characterized by 72% TLTT/28% TLT and 85% TLTT/15% TLT for the T/L and L/T deposition sequences, respectively. The overall TiO₂ adlayer coverages in these final structures (0.72 ± 0.05 ML for T/L and 0.85 ± 0.05 ML for L/T) are in reasonable agreement with the TiO₂ adlayer coverages found before deposition, suggesting that the TiO adlayers on the STO substrates have diffused to the surface over the course of the thin-film growth process.

As the through-thickness structure evolves during growth, we conducted time-resolved measurements at the $00\frac{1}{2}$ anti-Bragg peak during deposition to obtain insight into the dynamic rearrangement processes that take place at the surface. Figure 5 shows the scattering geometry, including the scattered intensities collected by an area detector and a slice of the background-subtracted data along the in-plane momentum transfer (q_{\parallel}) direction (inset). The scattered intensity can be divided into two components: specular (at $q_{\parallel} = 0$) and diffuse (at $q_{\parallel} \neq 0$) (43–45). The diffuse intensity originates from the presence of islands on the surface, with a profile that depends on the island distribution. It can be analyzed according to the following equation

$$I_{\text{diff}}(q) = \frac{I_0}{[1 + \xi^2(q - q_0)^2]^{3/2}} \quad (1)$$

which originates from a phenomenological model describing scattering from polydisperse, circular islands on a surface (45–47). Here, q_0 is the peak position (along q_{\parallel}) and ξ is a measure of the peak width (with larger ξ corresponding to a sharper peak). The parameter q_0 provides a measure of the mean interisland distance according to $d_{i-i} = 2\pi/q_0$. The diffuse scattering data were fit according to Eq. 1 after subtracting a constant background and the contribution from the specular intensity, as illustrated in Fig. 5.

The time-resolved scattering data at the $00\frac{1}{2}$ anti-Bragg peak are presented in Fig. 6, showing both the specular and diffuse intensities. The results for T/L deposition sequence are shown in Fig. 6 (A to C), with the shutter timing diagram provided in (Fig. 6A), slices along q_{\parallel} from -0.10 to 0 \AA^{-1} shown in (Fig. 6B), and the integrated specular (red) and diffuse intensities (green) shown in (Fig. 6C). As observed, diffuse intensity (Fig. 6B) is shown to emerge with LaO ML deposition (i.e., islands form) and then disappear with TiO_2 ML deposition (i.e., the surface smooths). Analysis of the specular reflectivity curves taken after LaO ML deposition (section S7) reveals that layer rearrangement occurs during and following the deposition of LaO, where the surface is characterized as a mixture of LTLT, LTT, LT, and TT model surface structures. In the fitting analysis, the total amounts of the deposited LaO layer and the second TiO_2 were constrained to be consistent with the experiment and the starting TiO_2 adlayer coverage on the bare STO substrate. This best-fit surface structure is also consistent with the formation of islands as indicated by the emergence of diffuse scatter. Information regarding the mean interisland distance d_{i-i} is provided in table S4. As can be seen in scans along q_{\parallel} shown in Fig. 6B, the peak position for the diffuse component shifts slightly toward $q_{\parallel} = 0$ over a period of ~ 5000 s, corresponding to a small increase in d_{i-i} from 9 to 10 nm.

The initial drop in the integrated specular intensity (red) shown in Fig. 6C results from roughening due to island formation upon LaO deposition; however, the intensity rises as the new structure forms on the

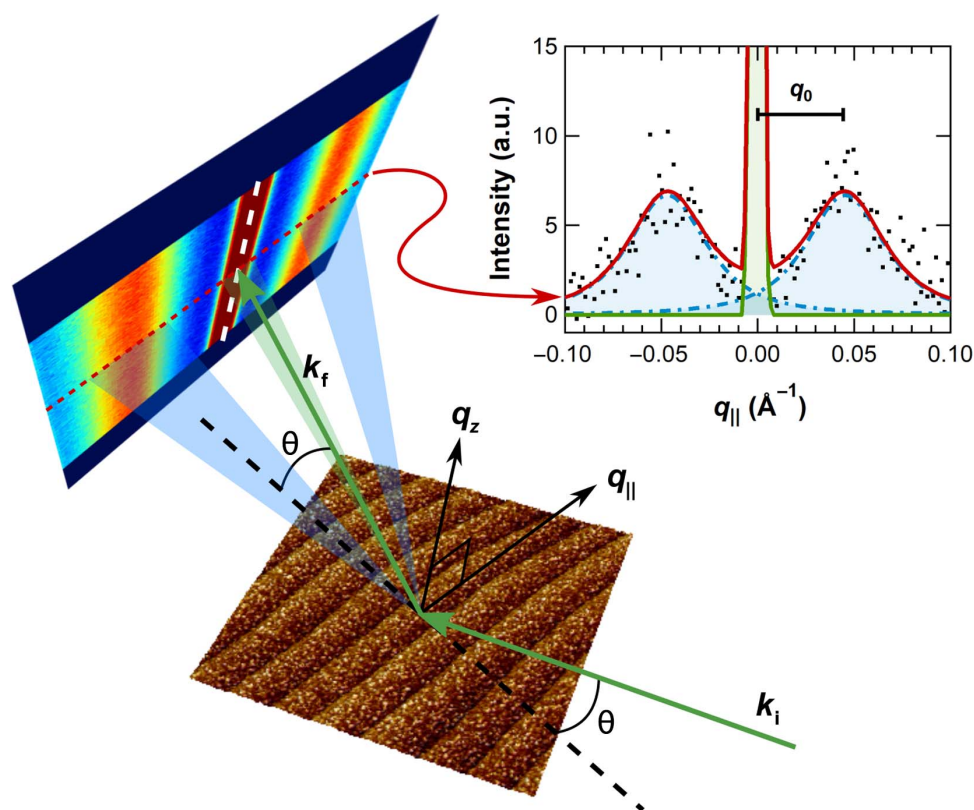


Fig. 5. Schematic illustration of the scattering geometry used in the time-resolved measurements of the specular and diffuse intensities during oxide MBE. The measurements were performed at the $00\frac{1}{2}$ anti-Bragg peak during the deposition processes, where the scattered intensities were collected by a Pilatus 100K area detector (detector image is shown after background subtraction). The plane of the incident (k_i) and scattered (k_f) wave vectors is set to be roughly perpendicular to the step edges. Specular and diffuse components could be seen, and slice of the data along the in-plane momentum transfer (q_{\parallel}) direction is shown in the inset plot, where the diffuse scattering lobe has a peak position at $q_{\parallel} = q_0$. The in situ scattering data and ex situ atomic force microscopy (AFM) image ($2 \mu\text{m} \times 2 \mu\text{m}$ scan area) are not related and are shown for demonstration purposes only. a.u., arbitrary units.

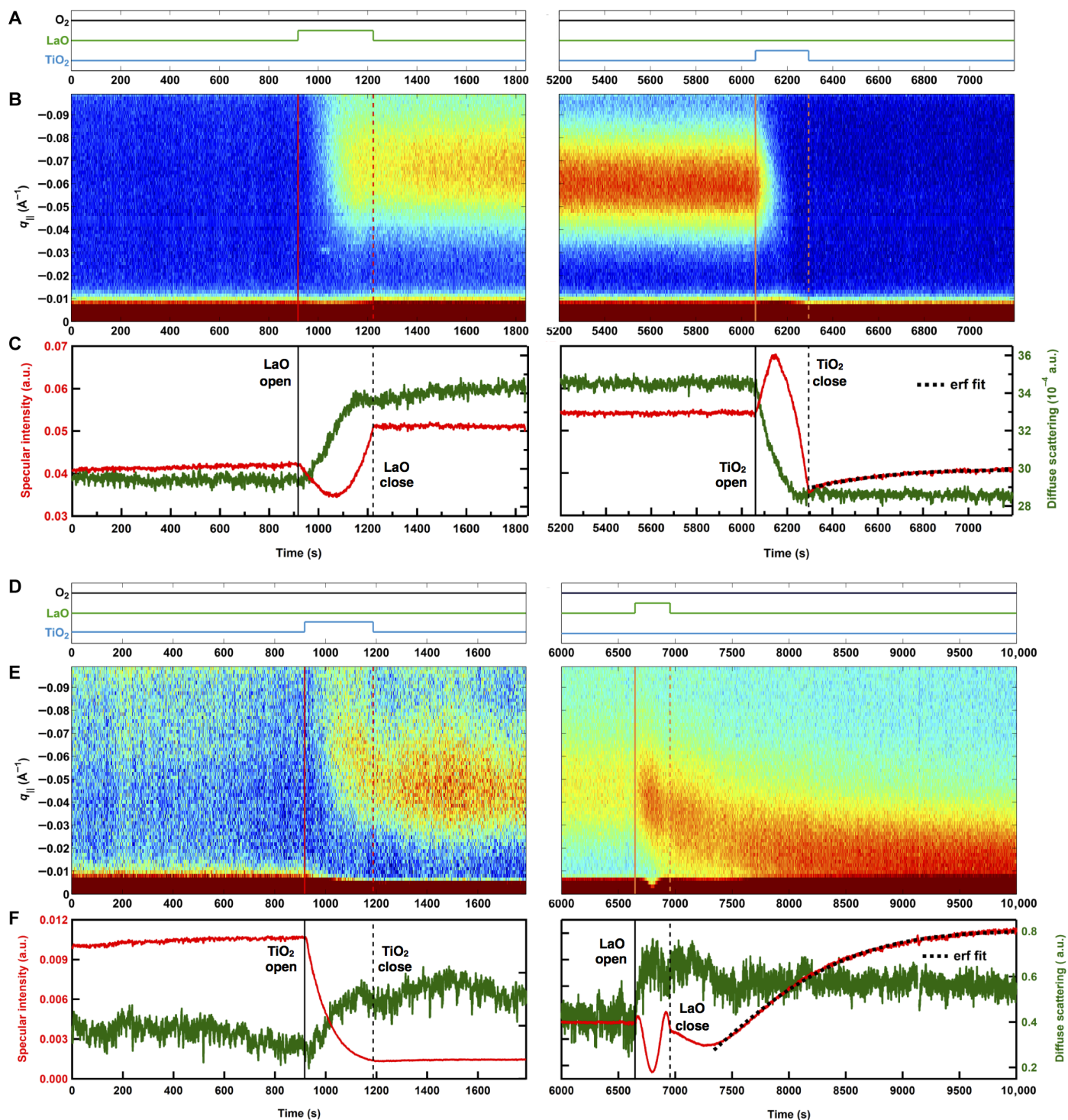


Fig. 6. Time-resolved measurements of the diffuse and specular intensities at the $00\frac{1}{2}$ anti-Bragg peak during oxide MBE. (A and B) Results for the T/L/STO #1 deposition sequence. (C and D) Results for the L/T/STO #2 deposition sequence. (E and F) False-color images of the scattered intensities, along with the timing diagrams indicating the deposited thin-film material. Solid and dashed vertical lines indicate the times at which the shutter was opened and closed, respectively. An empirical error function (erf) was fitted to each of the integrated specular intensities measured after the deposition of the final MLs to characterize the time scales of the relaxation behaviors [dashed black curves in (C) and (F)].

surface. The inverse behavior is observed upon TiO_2 deposition. The intensity continues to evolve after the TiO_2 shutter is closed (vertical dashed line), slowly relaxing over the course of ~ 900 s after TiO_2 deposition. There is no observed change in the diffuse intensity within the

same time interval. Together, these data indicate that the post-deposition behavior is due entirely to interlayer transport. We will elaborate on this after discussing the L/T deposition sequence, in which similar behavior is observed.

The deposition of the initial ML (TiO_2) in the L/T deposition sequence (Fig. 6, D to F) also leads to the emergence of a diffuse component, as shown in Fig. 6E. The results of fitting the diffuse intensity according to Eq. 1 are provided in table S4. In this case, no significant coarsening effect is observed between the two time scans, and the mean interisland distance, d_{i-1} , remains fixed at ~ 13.5 nm. The deposition of the LaO ML leads to an increase in the diffuse intensity, as shown in Fig. 6 (E and F), with the peak of the diffuse component q_0 shifting gradually toward the specular rod. The variations in q_0 and ξ are plotted in Fig. 7. Other than small artifacts in the data appearing when the La shutter is closed (vertical dashed lines), changes to the diffuse intensity continue to occur for at least another 500 s before plateauing. The mean interisland distance d_{i-1} increases from ~ 13.5 to ~ 41 nm over this time period (Fig. 7A), indicating substantial coarsening of the islands after deposition.

The specular component also exhibits time dependence (Fig. 6F, red curve). Similar to the behavior observed for the T/L deposition sequence, the scattered intensity of the specular component for the L/T deposition sequence slowly relaxes following the deposition of the final ML (TiO_2), after a brief transient between 7000 to 7300 s, albeit with a more pronounced variation in the intensity. To quantitatively compare the relaxation behaviors seen in the T/L and L/T deposition sequences following growth of the final MLs, the varying specular intensities were fit to an error function

$$I_{\text{spec}}(t) = A \operatorname{erf}\left(\frac{t - t_0}{\tau}\right) + I_{\text{BG}} \quad (2)$$

Least-squares fitting of this function gave satisfactory fits for both sets of specular intensity data (Fig. 6, C and F, dashed black curves). Besides the auxiliary prefactor A , time offset t_0 , and background I_{BG} terms, the main quantity of interest is the characteristic time constant τ .

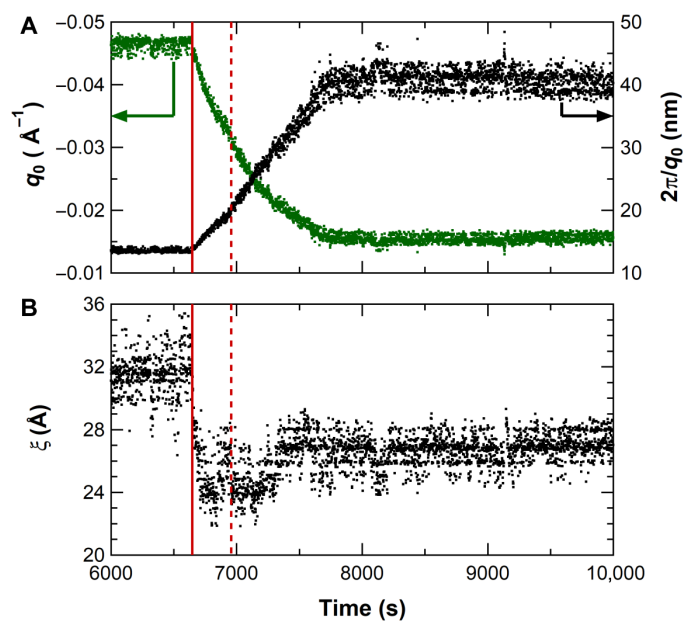


Fig. 7. Diffuse scattering fit parameters over the course of the final LaO ML deposition in the L/T/STO #2 deposition sequence. The peak position q_0 and a measure of the peak width ξ for the diffuse lobe near the $00\frac{1}{2}$ peak are extracted. The mean interisland distance, $d_{i-1} = 2\pi/q_0$, is also plotted.

We find $\tau_{\text{T/L}} = 748 \pm 12$ s for the T/L deposition sequence and $\tau_{\text{L/T}} = 1548 \pm 17$ s for the L/T deposition sequence, where the uncertainty is given by 1 SD. We discuss the physical meaning of these characteristic time constants in terms of atomic layer rearrangement behavior, as noted below.

The above results for the specular rod indicate that the overall atomic layer rearrangement results in the TTLT structure for the T/L deposition sequence and the same structure for the L/T deposition sequence. For the T/L deposition sequence, growth of the initial LaO ML on TiO_2 DL leads to a mixture of different structures, rather than the TLT structure that one may expect based on ideal perovskite stacking. This suggests that no thermodynamic preference or at least a large kinetic barrier exists to form the TLT structure under our growth conditions. This is in good agreement with the time-resolved diffuse scattering data, showing that intermixing of the deposited LaO layer and the preexisting TiO_2 adlayer leads to the formation of stable islands, with $d_{i-1} \sim 10$ nm.

The stable island structure disappears and reforms the smooth TiO_2 DL after the growth of one TiO_2 ML. The deposition of TiO_2 appears to trigger the atomic rearrangement behavior possibly because of the favorable energetics of the TiO_2 DL surface over the perovskite-like stackings of the surface atomic layers (TLT) and triple-layer TiO_2 (TTT) that would otherwise result. It is clear from the results of the L/T deposition sequence that the TiO_2 DL surface termination is preferred under the oxide thin-film growth conditions, wherein the LaO layer diffuses through two TiO_2 layers to achieve the final surface structure. This is reflected in the longer time constant for the relaxation behavior observed in the specular intensities after L/T deposition ($\tau_{\text{T/L}} = 1548 \pm 17$ s) versus T/L deposition ($\tau_{\text{T/L}} = 748 \pm 12$ s), in which some of the atomic layers have partially rearranged during the deposition of the first LaO ML.

Our observation of interlayer diffusion of the TiO_2 adlayer following thin-film deposition is consistent with the results of ex situ studies performed on PLD-grown thin films using scanning tunneling microscopy (48–50). This is rather remarkable, given the several fundamental differences in PLD versus MBE, including the deposition energies (51), the use of a stoichiometric target (PLD) versus the shuttered deposition of individual A and B site cations (MBE), and the oxygen pressures ($\sim \mu$ torr in oxide MBE versus \sim mtorr in PLD). These previous results and the results presented in this study suggest the universal tendency of the TiO_2 adlayer on bare STO (001) to diffuse toward the growth surface during thin-film deposition.

CONCLUSION

Analogous to surfactant-based epitaxial systems (52), we observe the presence of an oxide adlayer that tends toward the surface during the growth of perovskite heterostructures. This is shown through in situ SXR studies conducted during the deposition of LaTiO_3 on STO (001) by oxide MBE. The TiO_2 adlayer is a mixture of the $(\sqrt{13} \times \sqrt{13})R33.7^\circ$ and $(\sqrt{2} \times \sqrt{2})R45.0^\circ$ reconstructions but without long-range order, at least under growth conditions. We performed time-resolved SXR measurements during the growth of individual LaO and TiO_2 MLs on the TiO_2 DL-terminated (001) STO substrates using opposite deposition sequences, i.e., T/L versus L/T. The structures of the final surfaces were modeled using simple (1×1) structures derived from DFT, with similar TiO_2 adlayer coverages as those found on the bare STO substrates. These TiO_2 DL surface terminations were shown to reform despite the different deposition sequences, resulting in substantial differences in the evolution of island sizes and distributions, final surface

morphologies, and time scales of the diffusion process. Our results challenge commonly held assumptions regarding TiO₂-terminated STO (001) surfaces achieved by typical substrate preparation methods and reveal the critical role of excess TiO₂ surface stoichiometry on the initial stages of heteroepitaxial growth on this fundamental oxide substrate.

METHODS

(001) STO substrate surface preparation

Two low-miscut (<0.1°) 10 mm × 10 mm × 0.5 mm STO (001) crystals (CrysTec) were prepared using the procedure described in (2). The substrates were cleaned with solvents and deionized water, then etched in a buffered hydrofluoride solution (NH₄F/HF = 3:1) of pH 5 to 5.5, and annealed at 1050°C for 3 hours in flowing O₂ (200 standard cubic centimeters per minute). The surface morphologies obtained following this preparation procedure are shown by the tapping-mode atomic force microscopy (AFM) images in fig. S1. The substrates shown in fig. S1 (A and B) are used for the LaO-TiO₂ and TiO₂-LaO deposition sequences, respectively.

Oxide MBE with in situ SXRD

The thin-film growth and in situ SXRD measurements were performed using a custom-built oxide MBE chamber at beamline 33-ID-E of the Advanced Photon Source (APS) (53). The samples were heated and cooled using a temperature ramp rate of ±15°C/min under a background pressure of 1 × 10⁻⁷ torr O₂, and the thin-film deposition and SXRD measurements were performed at 700°C, as determined by an infrared optical pyrometer. LaO and TiO₂ were deposited using an effusion cell (Veeco) and a mini Ti-ball titanium sublimation source (Agilent Technologies), respectively. The source fluxes were calibrated using a quartz crystal microbalance and additionally calibrated by growing a 6-ML thin film of LaTiO₃ on a (001) STO substrate just before the in situ experiments, whose structure (lattice parameter and thickness) was verified by reflectivity measurements taken at room temperature immediately after cooling the sample. This confirmed that our growth conditions stabilized the perovskite LaTiO₃ phase as opposed to the La₂Ti₂O₇ phase observed at higher oxygen partial pressures (54).

A Pilatus 100K area detector was used to simultaneously measure the specular and diffuse intensities arising from scattering produced by x-rays with spot size given by 300 μm/sin θ horizontally and 400 μm vertically, where θ is the angle of incidence for the x-ray measured with respect to the sample surface. In performing the high-resolution specular reflectivity measurements, the step edges of the (001) STO substrate were aligned roughly parallel to the plane of incident and scattered x-ray wave vectors, as to project the sub-rods emanating from each Bragg peak because of the surface miscut under a single combined rod. In performing the time scans, the step edges of the (001) STO substrate were aligned roughly perpendicular to the plane of the incident and scattered x-ray wave vectors. This geometry allowed the in-plane component of the momentum transfer, $q_{||}$, to produce scattering that is directly related to the island correlations on the surface (43). The time scan measurements were sampled every second.

Density functional calculations

The model surface structures discussed in this work were derived using density functional calculations based on the (linearized augmented plane wave) (L)APW+lo method as implemented in the WIEN2K code

(55). Atomic positions were optimized using the modified Perdew-Burke-Ernzerhof functional (PBEsol) (56) implementation of the generalized gradient approximation. A 3D periodic surface slab model was created for each surface structure consisting of seven layers of the STO bulk (with a SrO layer surface termination) plus additional surface layers separated by 12 Å of vacuum, with inversion symmetry. Muffin-tin radii of 2.36, 1.90, 1.53, and 1.35 bohr were used for La, Sr, Ti, and O, respectively. The in-plane lattice parameter of these surface structures was based on the DFT-optimized bulk lattice parameter of STO (3.901 Å). All structures were relaxed until the force per atom, energy, and charge converged to within 0.1 eV/Å, 0.01 eV, and 0.005 *e*, respectively. The largest reciprocal lattice vector K_{\max} used in the plane wave expansion was given by $R_{\text{MT}}^{\text{min}} K_{\max} = 5.5$, where $R_{\text{MT}}^{\text{min}}$ is the smallest muffin-tin radius. The *k*-meshes were given by a single *k*-point in the irreducible wedge of the first Brillouin zone.

DFT-constrained fitting of specular reflectivity curves

To quantitatively determine the surface structures, the specular reflectivity curves were fit using a modified version of the DFT-constrained fitting procedure described in (36). In this procedure, a nonlinear least-squares fitting algorithm was used to allow the atoms to move away from their DFT minimum-energy positions to consider the effect of nonequilibrium processes, and the resulting Debye-Waller factors account for defects and disorder (36). Extending this approach, simultaneous fits to multiple DFT structures were performed so that both coherently and incoherently averaged linear combinations of the surface structures may be considered. Details of the fit procedure are described in section S2, and measures of the deviations of the fitted atomic positions from the DFT-derived minimum-energy positions and the goodness of fit are listed in tables S1 and S2 for the bare (001) STO substrates and for the thin-film structures, respectively. See the Supplementary Materials for detailed descriptions of the DFT-constrained fitting of the specular reflectivity curves and their fit parameters, additional experimental data, supporting figures, and tables.

SUPPLEMENTARY MATERIALS

Supplementary material for this article is available at <http://advances.sciencemag.org/cgi/content/full/5/4/eaav0764/DC1>

- Section S1. AFM images of prepared (001) STO substrates
- Section S2. Details of the DFT-constrained fitting of specular reflectivity curves
- Section S3. Calculated specular reflectivity curves of model STO (001) surfaces
- Section S4. Calculated specular reflectivity curves of model thin-film structures
- Section S5. Details of the SXRD characterization of the bare (001) substrates
- Section S6. Details of the SXRD characterization of the surface structures after the T/L and L/T deposition sequences
- Section S7. Details of the SXRD characterization of the surface structure after 1-ML LaO deposition
- Section S8. Determining the optimal weighting between the experimental data and DFT-derived structures
- Section S9. Determining the fraction of the coherent sum for the T/L and L/T reflectivity data
- Section S10. Fit parameters for the diffuse scattering component after deposition of the initial LaO and TiO₂ MLs
- Section S11. Ex situ AFM images taken after the T/L and L/T depositions
- Fig. S1. Surface morphologies of (001)-oriented STO substrates prepared using the etch-and-anneal method described in (2) by AFM.
- Fig. S2. Calculated specular reflectivity curves of single-layer SrO (1 × 1-S) and TiO₂ (1 × 1-T) surface terminations and TiO₂ DL (1 × 1-TT) surface termination.
- Fig. S3. Calculated specular reflectivity curves of several TiO₂ DL STO (001) surface reconstructions under 15.0-keV NR conditions and 16.1-keV R conditions for absorption at the Sr *K*-edge.
- Fig. S4. DFT-derived structures of possible layer sequences after deposition of LaO (L) and/or TiO₂ (T) ML(s) on a TiO₂ DL-terminated STO (001) surface and their calculated specular reflectivity curves.

Fig. S5. Fitted specular reflectivity curves taken after the LaO ML deposition in the T/L deposition sequence, in which the surface is modeled as a mixture of TLTL, TTL, TL, and TT model structures.

Fig. S6. Construction of a Pareto frontier to determine the optimal weighting between the experimental data and DFT-derived structures.

Fig. S7. Determination of the fraction of the coherent sum in fitting the specular reflectivity data for the T/L and L/T structures.

Fig. S8. Ex situ AFM images taken after the T/L and L/T deposition sequences.

Table S1. Measures of the deviations of the fitted atomic positions from the DFT-derived minimum-energy positions (z_{rms} and E_{dist}) and the goodness of fit (χ^2) for the bare (001) STO substrates modeled using the RT13 and RT2 reconstructions.

Table S2. Measures of the deviations of the fitted atomic positions from the DFT-derived minimum-energy positions (z_{rms} and E_{dist}) and the goodness of fit (χ^2) for the surfaces resulting after the T/L and L/T deposition sequences, modeled using the TLTT and TLT model structures.

Table S3. Measures of the deviations of the fitted atomic positions from the DFT-derived minimum-energy positions (z_{rms} and E_{dist}) and the goodness of fit (χ^2) for the final structures modeled as mixtures of the TLTL, TTL, TL, and TT surface structures.

Table S4. Fit parameters for the diffuse scattering component after depositing the initial LaO and TiO₂ MLs on each (001) STO substrate (STO #1 and STO #2).

References (57–61)

REFERENCES AND NOTES

- M. Kawasaki, K. Takahashi, T. Maeda, R. Tsuchiya, M. Shinohara, O. Ishiyama, T. Yonezawa, M. Yoshimoto, H. Koinuma, Atomic control of the SrTiO₃ crystal surface. *Science* **266**, 1540–1542 (1994).
- G. Koster, B. L. Kropman, G. J. H. M. Rijnders, D. H. A. Blank, H. Rogalla, Quasi-ideal strontium titanate crystal surfaces through formation of strontium hydroxide. *Appl. Phys. Lett.* **73**, 2920–2922 (1998).
- M. Kareev, S. Prosandeev, J. Liu, C. Gan, A. Kareev, J. W. Freeland, M. Xiao, J. Chakhalian, Atomic control and characterization of surface defect states of TiO₂ terminated SrTiO₃ single crystals. *Appl. Phys. Lett.* **93**, 061909 (2008).
- A. Biswas, P. B. Rossen, C.-H. Yang, W. Siemons, M.-H. Jung, I. K. Yang, R. Ramesh, Y. H. Jeong, Universal Ti-rich termination of atomically flat SrTiO₃ (001), (110), and (111) surfaces. *Appl. Phys. Lett.* **98**, 051904 (2011).
- B. Prakash, S. Chakraverty, Realization of atomically flat steps and terraces like surface of SrTiO₃ (001) single crystal by hot water etching and high temperature annealing. *Solid State Commun.* **213–214**, 28–30 (2015).
- D. G. Schlom, L.-Q. Chen, X. Pan, A. Schmehl, M. A. Zurbuchen, A thin film approach to engineering functionality into oxides. *J. Am. Ceram. Soc.* **91**, 2429–2454 (2008).
- E. J. Monkman, C. Adamo, J. A. Mundy, D. E. Shai, J. W. Harter, D. Shen, B. Burganov, D. A. Muller, D. G. Schlom, K. M. Shen, Quantum many-body interactions in digital oxide superlattices. *Nat. Mater.* **11**, 855–859 (2012).
- Y. F. Nie, Y. Zhu, C.-H. Lee, L. F. Kourkoutis, J. A. Mundy, J. Junquera, P. Ghosez, D. J. Baek, S. Sung, X. X. Xi, K. M. Shen, D. A. Muller, D. G. Schlom, Atomically precise interfaces from non-stoichiometric deposition. *Nat. Commun.* **5**, 4530 (2014).
- A. Ohtomo, D. A. Muller, J. L. Grazul, H. Y. Hwang, Artificial charge-modulation in atomic-scale perovskite titanate superlattices. *Nature* **419**, 378–380 (2002).
- M. Takizawa, H. Wadati, K. Tanaka, M. Hashimoto, T. Yoshida, A. Fujimori, A. Chikamatsu, H. Kumigashira, M. Oshima, K. Shibuya, T. Mihara, T. Ohnishi, M. Lippmaa, M. Kawasaki, H. Koinuma, S. Okamoto, A. J. Millis, Photoemission from buried interfaces in SrTiO₃/LaTiO₃ superlattices. *Phys. Rev. Lett.* **97**, 057601 (2006).
- A. Ohtomo, H. Y. Hwang, A high-mobility electron gas at the LaAlO₃/SrTiO₃ heterointerface. *Nature* **427**, 423–426 (2004).
- Y. Chen, N. Pryds, J. E. Kleibauer, G. Koster, J. Sun, E. Stamate, B. Shen, G. Rijnders, S. Linderoth, Metallic and insulating interfaces of amorphous SrTiO₃-based oxide heterostructures. *Nano Lett.* **11**, 3774–3778 (2011).
- G. Herranz, F. Sánchez, N. Dix, M. Scigaj, J. Fontcuberta, High mobility conduction at (110) and (111) LaAlO₃/SrTiO₃ interfaces. *Sci. Rep.* **2**, 758 (2012).
- P. Moetakef, J. Y. Zhang, A. Kozhanov, B. Jalan, R. Seshadri, S. J. Allen, S. Stemmer, Transport in ferromagnetic GdTiO₃/SrTiO₃ heterostructures. *Appl. Phys. Lett.* **98**, 112110 (2011).
- Y. Z. Chen, N. Bovet, F. Trier, D. V. Christensen, F. M. Qu, N. H. Andersen, T. Kasama, W. Zhang, R. Giraud, J. Dufouleur, T. S. Jespersen, J. R. Sun, A. Smith, J. Nygård, L. Lu, B. Büchner, B. G. Shen, S. Linderoth, N. Pryds, A high-mobility two-dimensional electron gas at the spinel/perovskite interface of γ -Al₂O₃/SrTiO₃. *Nat. Commun.* **4**, 1371 (2013).
- Z. Q. Liu, C. J. Li, W. M. Lü, X. H. Huang, Z. Huang, S. W. Zeng, X. P. Qiu, L. S. Huang, A. Annadi, J. S. Chen, J. M. D. Coey, T. Venkatesan, Ariando, Origin of the two-dimensional electron gas at LaAlO₃/SrTiO₃ interfaces: The role of oxygen vacancies and electronic reconstruction. *Phys. Rev. X* **3**, 021010 (2013).
- H. Lee, N. Campbell, J. Lee, T. J. Asel, T. R. Paudel, H. Zhou, J. W. Lee, B. Noesges, J. Seo, B. Park, L. J. Brillson, S. H. Oh, E. Y. Tsybal, M. S. Rzczowski, C. B. Eom, Direct observation of a two-dimensional hole gas at oxide interfaces. *Nat. Mater.* **17**, 231–236 (2018).
- N. Reyren, S. Thiel, A. D. Caviglia, L. F. Kourkoutis, G. Hammerl, C. Richter, C. W. Schneider, T. Kopp, A.-S. Rüetschi, D. Jaccard, M. Gabay, D. A. Muller, J.-M. Triscone, J. Mannhart, Superconducting interfaces between insulating oxides. *Science* **317**, 1196–1199 (2007).
- S. Stemmer, S. James Allen, Two-dimensional electron gases at complex oxide interfaces. *Annu. Rev. Mater. Res.* **44**, 151–171 (2014).
- S. Thiel, G. Hammerl, A. Schmehl, C. W. Schneider, J. Mannhart, Tunable quasi-two-dimensional electron gases in oxide heterostructures. *Science* **313**, 1942–1945 (2006).
- T. C. Asmara, A. Annadi, I. Santoso, P. K. Gogoi, A. Kotlov, H. M. Omer, M. Motapothula, M. B. H. Breese, M. Rübhausen, T. Venkatesan, Ariando, A. Rusydi, Mechanisms of charge transfer and redistribution in LaAlO₃/SrTiO₃ revealed by high-energy optical conductivity. *Nat. Commun.* **5**, 3663 (2014).
- H. W. Jang, D. A. Felker, C. W. Bark, Y. Wang, M. K. Niranjan, C. T. Nelson, Y. Zhang, D. Su, C. M. Folkman, S. H. Baek, S. Lee, K. Janicka, Y. Zhu, X. Q. Pan, D. D. Fong, E. Y. Tsybal, M. S. Rzczowski, C. B. Eom, Metallic and insulating oxide interfaces controlled by electronic correlations. *Science* **331**, 886–889 (2011).
- S. Tan, Y. Zhang, M. Xia, Z. Ye, F. Chen, X. Xie, R. Peng, D. Xu, Q. Fan, H. Xu, J. Jiang, T. Zhang, X. Lai, T. Xiang, J. Hu, B. Xie, D. Feng, Interface-induced superconductivity and strain-dependent spin density waves in FeSe/SrTiO₃ thin films. *Nat. Mater.* **12**, 634–640 (2013).
- J.-F. Ge, Z.-L. Liu, C. Liu, C.-L. Gao, D. Qian, Q.-K. Xue, Y. Liu, J.-F. Jia, Superconductivity above 100 K in single-layer FeSe films on doped SrTiO₃. *Nat. Mater.* **14**, 285–289 (2014).
- D. M. Kienzle, L. D. Marks, Surface transmission electron diffraction for SrTiO₃ surfaces. *CrystEngComm* **14**, 7833–7839 (2012).
- N. Erdman, K. R. Poepplmeier, M. Asta, O. Warschkow, D. E. Ellis, L. D. Marks, The structure and chemistry of the TiO₂-rich surface of SrTiO₃ (001). *Nature* **419**, 55–58 (2002).
- Y. Lin, A. E. Becerra-Toledo, F. Silly, K. R. Poepplmeier, M. R. Castell, L. D. Marks, The (2 × 2) reconstructions on the SrTiO₃ (001) surface: A combined scanning tunneling microscopy and density functional theory study. *Surf. Sci.* **605**, L51–L55 (2011).
- N. Erdman, O. Warschkow, M. Asta, K. R. Poepplmeier, D. E. Ellis, L. D. Marks, Surface structures of SrTiO₃(001): A TiO₂-rich reconstruction with a c(4 × 2) unit cell. *J. Am. Chem. Soc.* **125**, 10050–10056 (2003).
- D. M. Kienzle, A. E. Becerra-Toledo, L. D. Marks, Vacant-site octahedral tilings on SrTiO₃(001), the ($\sqrt{13} \times \sqrt{13}$)R33.7° surface, and related structures. *Phys. Rev. Lett.* **106**, 176102 (2011).
- J. Ciston, H. G. Brown, A. J. D'Alfonso, P. Koirala, C. Ophus, Y. Lin, Y. Suzuki, H. Inada, Y. Zhu, L. J. Allen, L. D. Marks, Surface determination through atomically resolved secondary-electron imaging. *Nat. Commun.* **6**, 7358 (2015).
- R. Herger, P. R. Willmott, O. Bunk, C. M. Schlepütz, B. D. Patterson, B. Delley, Surface of strontium titanate. *Phys. Rev. Lett.* **98**, 076102 (2007).
- S. Cook, L. D. Marks, Ab initio predictions of double-layer TiO₂-terminated SrTiO₃(001) surface reconstructions. *J. Phys. Chem. C* **122**, 21991–21997 (2018).
- Y. Tokura, Y. Taguchi, Y. Okada, Y. Fujishima, T. Arima, K. Kumagai, Y. Iye, Filling dependence of electronic properties on the verge of metal–Mott-insulator transition in Sr_{1-x}La_xTiO₃. *Phys. Rev. Lett.* **70**, 2126–2129 (1993).
- H. Y. Hwang, Y. Iwasa, M. Kawasaki, B. Keimer, N. Nagaosa, Y. Tokura, Emergent phenomena at oxide interfaces. *Nat. Mater.* **11**, 103–113 (2012).
- P. Fenter, C. Park, Termination interference along crystal truncation rods of layered crystals. *J. Appl. Crystallogr.* **37**, 977–987 (2004).
- M. Plaza, X. Huang, J. Y. P. Ko, M. Shen, B. H. Simpson, J. Rodríguez-López, N. L. Ritzert, K. Letchworth-Weaver, D. Gunceler, D. G. Schlom, T. A. Arias, J. D. Brock, H. D. Abruña, Structure of the photo-catalytically active surface of SrTiO₃. *J. Am. Chem. Soc.* **138**, 7816–7819 (2016).
- O. Warschkow, M. Asta, N. Erdman, K. R. Poepplmeier, D. E. Ellis, L. D. Marks, TiO₂-rich reconstructions of SrTiO₃(001): A theoretical study of structural patterns. *Surf. Sci.* **573**, 446–456 (2004).
- J. Biscaras, N. Bergeal, A. Kushwaha, T. Wolf, A. Rastogi, R. C. Budhani, J. Lesueur, Two-dimensional superconductivity at a Mott insulator/band insulator interface LaTiO₃/SrTiO₃. *Nat. Commun.* **1**, 89 (2010).
- J. Biscaras, N. Bergeal, S. Hurand, C. Grossetête, A. Rastogi, R. C. Budhani, D. LeBoeuf, C. Proust, J. Lesueur, Two-dimensional superconducting phase in LaTiO₃/SrTiO₃ heterostructures induced by high-mobility carrier doping. *Phys. Rev. Lett.* **108**, 247004 (2012).
- S. Caprara, J. Biscaras, N. Bergeal, D. Bucheli, S. Hurand, C. Feuillet-Palma, A. Rastogi, R. C. Budhani, J. Lesueur, M. Grilli, Multiband superconductivity and nanoscale inhomogeneity at oxide interfaces. *Phys. Rev. B* **88**, 020504 (2013).
- Y. J. Chang, L. Moreschini, A. Bostwick, G. A. Gaines, Y. S. Kim, A. L. Walter, B. Freelon, A. Tebano, K. Horn, E. Rotenberg, Layer-by-layer evolution of a two-dimensional electron gas near an oxide interface. *Phys. Rev. Lett.* **111**, 126401 (2013).

42. J. H. Ngai, F. J. Walker, C. H. Ahn, Correlated oxide physics and electronics. *Annu. Rev. Mater. Res.* **44**, 1–17 (2014).
43. J. D. Ferguson, G. Arikian, D. S. Dale, A. R. Woll, J. D. Brock, Measurements of surface diffusivity and coarsening during pulsed laser deposition. *Phys. Rev. Lett.* **103**, 256103 (2009).
44. J. D. Brock, J. D. Ferguson, A. R. Woll, X-ray scattering studies of the surface structure of complex oxide films during layer-by-layer growth via pulsed laser deposition. *Metall. Mater. Trans. A* **41**, 1162–1166 (2010).
45. J. D. Brock, J. D. Ferguson, Y. Kim, H.-Q. Wang, A. R. Woll, Nucleation, coarsening, and coalescence during layer-by-layer growth of complex oxides via pulsed laser deposition: Time-resolved, diffuse x-ray scattering studies. *Mater. Sci. Eng. A* **528**, 72–76 (2010).
46. A. Guiner, G. Fournet, C. B. Walker, K. L. Yudowitch, *Small Angle Scattering of X-rays* (Wiley & Sons, 1955).
47. G. Porod, General theory, in *Small Angle X-ray Scattering*, O. Glatter, O. Kratky, Eds. (Academic Press, 1982), pp. 17–51.
48. R. Shimizu, K. Iwaya, T. Ohsawa, S. Shiraki, T. Hasegawa, T. Hashizume, T. Hitosugi, Atomic-scale visualization of initial growth of homoepitaxial SrTiO₃ thin film on an atomically ordered substrate. *ACS Nano* **5**, 7967–7971 (2011).
49. R. Shimizu, T. Ohsawa, K. Iwaya, S. Shiraki, T. Hitosugi, Epitaxial growth process of La_{0.7}Ca_{0.3}MnO₃ thin films on SrTiO₃(001): Thickness-dependent inhomogeneity caused by excess Ti atoms. *Cryst. Growth Des.* **14**, 1555–1560 (2014).
50. T. Ohsawa, M. Saito, I. Hamada, R. Shimizu, K. Iwaya, S. Shiraki, Z. Wang, Y. Ikuhara, T. Hitosugi, A single-atom-thick TiO₂ nanomesh on an insulating oxide. *ACS Nano* **9**, 8766–8772 (2015).
51. J. J. Cuomo, D. L. Pappas, J. Bruley, J. P. Doyle, K. L. Saenger, Vapor deposition processes for amorphous carbon films with sp³ fractions approaching diamond. *J. Appl. Phys.* **70**, 1706–1711 (1991).
52. E. Tournié, K. H. Ploog, Surfactant-mediated molecular beam epitaxy of strained layer semiconductor heterostructures. *Thin Solid Films* **231**, 43–60 (1993).
53. J. H. Lee, I. C. Tung, S.-H. Chang, A. Bhattacharya, D. D. Fong, J. W. Freeland, H. Hong, In situ surface/interface x-ray diffractometer for oxide molecular beam epitaxy. *Rev. Sci. Instrum.* **87**, 013901 (2016).
54. A. Ohtomo, D. A. Muller, J. L. Grazul, H. Y. Hwang, Epitaxial growth and electronic structure of LaTiO₃ films. *Appl. Phys. Lett.* **80**, 3922–3924 (2002).
55. P. Blaha, K. Schwarz, G. Madsen, D. Kvasnicka, J. Luitz, R. Laskowski, F. Tran, L. D. Marks, *WIEN2k: An Augmented Plane Wave Plus Local Orbitals Program for Calculating Crystal Properties* (Technische Universität Wien, 2018).
56. J. P. Perdew, A. Ruzsinszky, G. I. Csonka, O. A. Vydrov, G. E. Scuseria, L. A. Constantin, X. Zhou, K. Burke, Restoring the density-gradient expansion for exchange in solids and surfaces. *Phys. Rev. Lett.* **100**, 136406 (2008).
57. R. O. Bell, G. Rupprecht, Elastic constants of strontium titanate. *Phys. Rev.* **129**, 90–94 (1963).
58. P. J. Brown, A. G. Fox, E. N. Maslen, M. A. O’Keefe, B. T. M. Willis, in *International Tables for Crystallography Volume C: Mathematical, Physical and Chemical Tables*, E. Prince, Ed. (Springer Netherlands, 2004), pp 554–595.
59. W. G. Stirling, R. Currat, Experimental verification of the phonon dispersion curves of strontium titanate. *J. Phys. C Solid State Phys.* **9**, L519 (1976).
60. G. Ju, M. J. Highland, C. Thompson, J. A. Eastman, P. H. Fuoss, H. Zhou, R. Dejus, G. Brian, Characterization of the x-ray coherence properties of an undulator beamline at the Advanced Photon Source. *J. Synchrotron. Radiat.* **25**, 1036–1047 (2018).
61. T. A. Petach, A. Mehta, M. F. Toney, D. Goldhaber-Gordon, Crystal truncation rods from miscut surfaces. *D. Phys. Rev. B* **95**, 184104 (2017).

Acknowledgments

Funding: The work by S.C., T.K.A., and D.D.F. was supported by the U.S. Department of Energy (DOE), Office of Science, Basic Energy Sciences (BES), Materials Science and Engineering Division. The work by L.D.M. was supported by the DOE, Office of Science, BES, under award no. DE-FG02-01ER45945. The use of the APS and Center for Nanoscale Materials, Office of Science User Facilities, was supported by the U.S. DOE, Office of Science, BES, under contract no. DE-AC02-06CH11357. **Author contributions:** S.C., T.K.A., L.D.M., and D.D.F. conceived the experiment. S.C., T.K.A., I.-C.T., H.H., and D.D.F. carried out the experiment at the APS. S.C., T.K.A., I.-C.T., and D.D.F. analyzed the experimental data. K.L.-W. performed the theoretical modeling. S.C., L.D.M., and D.D.F. wrote the manuscript with contributions from all the other authors. **Competing interests:** The authors declare that they have no competing interests. **Data and materials availability:** All data needed to evaluate the conclusions in the paper are present in the paper and/or the Supplementary Materials. Additional data related to this paper may be requested from the authors.

Submitted 11 August 2018

Accepted 14 February 2019

Published 12 April 2019

10.1126/sciadv.aav0764

Citation: S. Cook, K. Letchworth-Weaver, I.-C. Tung, T. K. Andersen, H. Hong, L. D. Marks, D. D. Fong, How heteroepitaxy occurs on strontium titanate. *Sci. Adv.* **5**, eaav0764 (2019).

How heteroepitaxy occurs on strontium titanate

Seyoung Cook, Kendra Letchworth-Weaver, I-Cheng Tung, Tassie K. Andersen, Hawoong Hong, Laurence D. Marks and Dillon D. Fong

Sci Adv 5 (4), eaav0764.
DOI: 10.1126/sciadv.aav0764

ARTICLE TOOLS

<http://advances.sciencemag.org/content/5/4/eaav0764>

SUPPLEMENTARY MATERIALS

<http://advances.sciencemag.org/content/suppl/2019/04/08/5.4.eaav0764.DC1>

REFERENCES

This article cites 57 articles, 4 of which you can access for free
<http://advances.sciencemag.org/content/5/4/eaav0764#BIBL>

PERMISSIONS

<http://www.sciencemag.org/help/reprints-and-permissions>

Use of this article is subject to the [Terms of Service](#)

Science Advances (ISSN 2375-2548) is published by the American Association for the Advancement of Science, 1200 New York Avenue NW, Washington, DC 20005. 2017 © The Authors, some rights reserved; exclusive licensee American Association for the Advancement of Science. No claim to original U.S. Government Works. The title *Science Advances* is a registered trademark of AAAS.